Characterization and Modeling of a Bulk Acoustic Wave Particle Focusing Device

Surendra K. Ravula*, Darren W. Branch, Karl Westlake, Igal Brener
Applied Photonic Microsystems
Sandia National Laboratories
Albuquerque, NM, USA
*Corresponding author email: skravul@sandia.gov

Abstract— **In this paper, we discuss our work in the modeling and characterization of an acoustic-microfluidic focusing device that uses standing bulk acoustic waves to focus particles under flow. Modeling was done using Comsol Multiphysics® (Comsol, Los Angeles, CA), a multiphysics FEM tool, and the performance of the device was assessed through coefficient of variance (CV) measurements using a confocal microscope.**

I. INTRODUCTION

Acoustic manipulation and focusing technologies have matured in the last ten years to allow more sophisticated handling of particles in microsystems[1-5]. Acoustic force manipulation allows a well-understood and reliable way to move groups of particles in microchannels. Here suspended particles exposed to an ultrasound standing wave field will move the particles toward either the pressure nodes or the pressure antinodes depending on the density and compressibility of the particles and medium. The coupling of the acoustic force to the microfluidic structure also allows for these forces to span the entire dimensions of large (hundreds of μm) fluidic channels. Moreover, the forces can be spatially decoupled to strengthen primary radiation forces in one dimension and reduce those in other directions. To achieve good particle focusing, the sidewalls reflecting the acoustic wave must have low surface roughness and the channel must be multiples of one-half wavelength. The driving frequency of the piezoelectric slab is then tuned to create a standing wave of one half wavelength.

In this paper, we discuss the fabrication, characterization, and modeling of a focusing device that uses acoustic standing waves to focus particles within microfluidic channels. The device is made from a two step deep reactive ion etching (DRIE) process and its focusing performance is quantified by making coefficient of variance (CV) measurements using a confocal microscope. Finally, to aid in analyzing and improving device performance, the finite element method (FEM) is used to plot the acoustic radiation pressure profile within the structure as the frequency is tuned. In the end, this device can be integrated with other cytometry components into a lab on a chip system that can be a portable, low-cost alternative to conventional cytometry systems.

II. METHODS

A. Fabrication of the Device

A square cross section microchannel (214μm) and corresponding through wafer ports were created in silicon using a two mask DRIE Bosch etch process. The channel dimensions (214μm width and height) were chosen such that they set up acoustic standing waves of one-half wavelength both laterally and vertically within the cavity when actuated at 3.5MHz (see Figure 1 and Figure 2). A piezoelectric transducer (BM400, Sensor Technology Limited, Collingwood, Ontario) was glued to the underside of the silicon substrate to couple acoustic energy into the channel. A glass coverslip (quarter-wavelength thickness) was anodically bonded to the top of the silicon microfluidic manifold to create an acoustic reflector and to allow optical access to the flowing particles within the channels. Nanoport assemblies and tubing (Upchurch Scientific, Oak Harbor, WA) were attached to the underside of the wafer to provide fluidic access. An Agilent 33220A function generator attached to an RF power amplifier
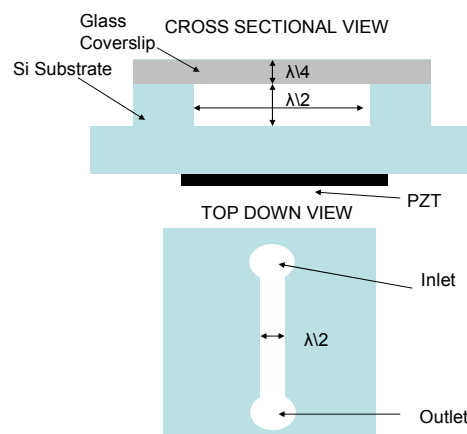

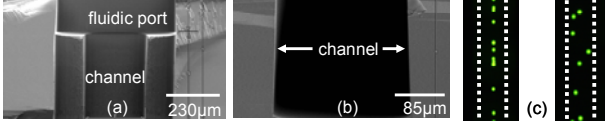Figure 1. Schematic of acoustic focusing device.

Figure 2. Fabricated acoustic focusing device and particle focusing. The microfluidic device is made from a two step DRIE process (a) Cross-sectional view of the through wafer port intersecting with the microfluidic channel. (b) Cross-sectional view of the microfluidic channel. (c) 10μm fluorescent beads in both focused and unfocused streams within the resonant acoustic cavity.

(ENI Model 2100L) was used to drive the piezo circuit, and a syringe pump (Harvard Apparatus PHD 2000 programmable, Holliston, MA) was used to deliver particles to the resonant microfluidic cavities.

B. Testing of Focusing

Initially, coefficient of variance measurements were done to understand positional spread of focused 10μm particles within the resonant cavity using a custom-built confocal microscope (see Figure 3) with a photomultiplier tube (PMT) detector (Hamamatsu Model H6779). Coefficients of variance were calculated by taking a 500 bead sample for each operating point (transducer drive voltage, frequency, and flow rate) and dividing the standard deviation of the peak deflection heights outputted by the photomultiplier tube by their mean. Data sets were analyzed in MATLAB. Here, a 20mW Cyan 488nm laser head (Picarro, Sunnyvale, CA) was used to excite 10μm fluorescent particles (Spherotech, Lake Forest, IL). The acoustic device sat on a movable three-axis stage under a 10X objective. A FITC filter cube (Series 41001) (Chroma Technology, Rockingham, VT) was inserted into a Navitar (Rochester, NY) cube cage. Extension tubes (Thorlabs, Newton, NJ) were used to couple laser light to the objective, to a camera (JAI CV M50, San Jose, CA), and to the PMT through a pinhole. The signal from the PMT was routed
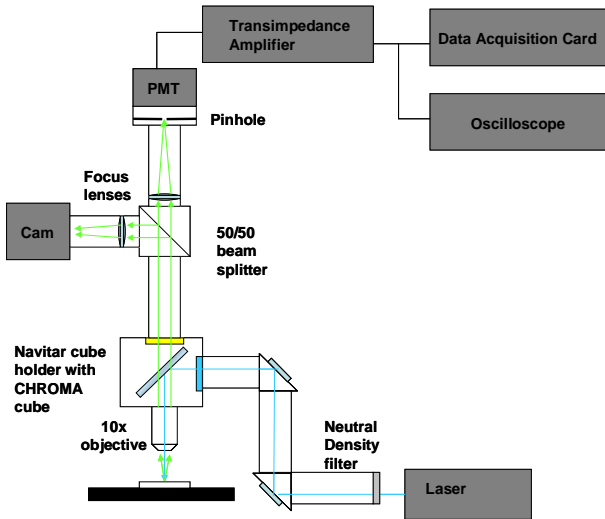

Figure 3. Confocal microscope for coefficient of variance measurements.

through a transimpedance amplifier (Stanford Research Systems, Model SR570) and to a storage oscilloscope (Agilent 54624A).

III. THEORETICAL ANALYSIS

A. Piezoelectric Theory

In the FEM formalism for piezoelectric media Newton's law relates the stresses to the particle displacement and electric displacement to the free volume charge density as

$$\nabla \cdot T_{6x1} + f = \rho \ddot{u} \tag{1}$$

$$\nabla \cdot D = \sigma \tag{2}$$

where T is the mechanical stress tensor (N/m^2), f is a mechanical body force (N/m^3), ρ is the mass density (kg/m^3), u is the displacement (m), D is the electric displacement (C/m^2) and σ is the free volume charge density (C/m^3). The strain displacement relationship is given as

$$S_{6x1} = \nabla_s u \tag{3}$$

where S is the strain column vector and u is the displacement (m). The piezoelectric constitutive equations that couple the mechanical and electrical quantities in the piezoelectric material are expressed in matrix notation as

$$T_{6x1} = c_{6x6}^E S_{6x1} - e_{6x3}^T \nabla \phi_{3x1} \tag{4}$$

$$D_{3x1} = e_{3x6} S_{6x1} + \varepsilon_{3x3}^S \nabla \phi_{3x1} \tag{5}$$

where T is the stress column vector, S is the strain column vector, ϕ is the electric potential (V), e is the piezoelectric matrix (C/m^2), c^E is the elastic stiffness matrix at constant electric field (N/m^2), and ε^s is the dielectric permittivity matrix at constant strain (F/m). The superscript T is the transpose of a matrix. In (4) and (5) the quasi-static approximation, $E = -\nabla \phi$, is applicable for acoustic waves. For a unique solution the mechanical displacement or stress and electrical potential or electric displacement boundary conditions are imposed on the entire boundary of the problem. The boundary conditions combined with 1 through 5 completely determine the motion of the piezoelectric material.

B. Acoustic Pressure Field

In the fluid the acoustic waves are governed by the frequency-domain Helmholtz equation for determining the acoustic pressure,

$$\nabla \cdot \left(-\frac{1}{\rho_f} (\nabla p - q) \right) - \left(\frac{\omega^2}{\rho_f c_f^2} \right) p = Q \tag{6}$$

where p is the acoustic pressure (Pa), ρ_f is the fluid density (kg/m^3), c_f is the complex acoustic velocity (m/s) in the medium, ω is the angular frequency (rad/s), q is a dipole source term (N/m^3), and Q is the monopole source term (1/s^2). The inclusion of acoustic loss in the fluid region is introduced

by allowing the fluid density (ρ_f) and acoustic speed (c_f) to be complex quantities,

$$\rho_f = \frac{Z_f k_f}{\omega} \qquad c_f = \frac{\omega}{k_f} \qquad k_f = \frac{\omega}{c_s} - i\alpha \qquad Z_f = \rho_o c_s \qquad (7)$$

where Z_f is the complex acoustic impedance (Pa·s/m^2), α is the attenuation coefficient (1/m), c_s is the acoustic speed in the fluid (m/s) and ρ_o is the fluid density (kg/m^3). In the absence of damping (i.e. $\alpha = 0$), $\rho_f = \rho_o$ and $c_f = c_s$.

C. Boundary Conditions

The piezoelectric transducer was excited by application of 25V to the bottom edge while the top surface had V = 0, where the electrodes were modeled as infinitely thin (see Figure 4). The edges of the transducer were fixed with the electrode surfaces allowed to move freely to approximate a real transducer. The top and bottom surface of the transducer were free to move. Continuity of stresses and displacements were imposed on the internal boundaries of the silicon, piezoelectric transducer and Pyrex layers. The motion of the solid regions produces normal acceleration at the interfaces between the fluid and silicon layer given as

$$a_x \cdot n_x + a_y \cdot n_y = n \cdot \left(\frac{1}{\rho_f} (\nabla p) \right) \qquad (8)$$

where the a_i's are the acceleration at the fluid-structure interface (m/s^2), ρ_f is the complex fluid density, and p is the pressure in the fluid layer. This equation couples the motion of the transducer and silicon layer into acceleration of the fluid. In turn the fluid pressure produces a load on the silicon and Pyrex regions. This load was included since the fluid pressure is not negligible as in the case of an air domain in contact with the silicon. The impact of the fluid loading would be further reduced at high driving potentials in excess of 100V. Fluid loads the silicon and Pyrex layers as

$$F_x = -p \cdot n_x$$
$$F_y = -p \cdot n_y \qquad (9)$$

where F is the force, p is the pressure in the fluid (Pa), and n_x and n_y are the normal components at the fluid-structure interfaces.

At the interface between the fluid and Pyrex layer, two cases were considered to assess the impact of boundary as an acoustic reflector. In the case of a perfectly rigid interface the normal derivative of the pressure must vanish,
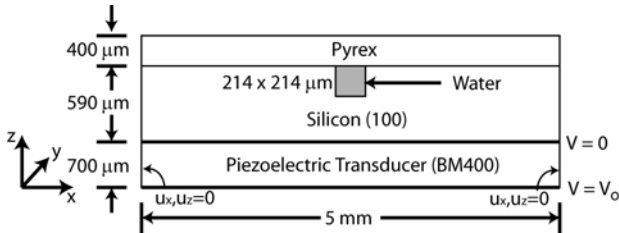
$$\frac{\partial p}{\partial n} = 0 \qquad (10)$$

This condition is only valid if the dipole source term is zero in the fluid region which in this model there are no acoustic sources present in the fluid region. This is the case for a rigid interface where the normal component of the velocity vanishes. The second case has a $\lambda/4$ Pyrex reflector to determine the efficacy of the reflector.

IV. MODELING RESULTS

A. 2D Acoustic Pressure Field in Microchannel using a Ideal Reflector

To determine the efficacy of the acoustic reflector, the boundary condition between the fluid region and Pyrex was defined to be ideal i.e. $\partial p / \partial n = 0$. This condition forces the velocity at the boundary to be zero while allowing the pressure to have a non-zero value in the standing wave cavity. The acoustic pressure field in the fluid region as shown in Figure 5 exhibited frequency dependant effects. In this design the transducer anti-resonance frequency was 3.35 MHz with a resonance at 3.8 MHz. In the fluid region, the $\lambda/2$ cavity height was 214 μm at an excitation of 3.5 MHz. At 3.528 MHz, a well defined central node is observed in the fluid channel. Nodal confinement was highly sensitive to frequency, where a frequency shift of 2 kHz produced a well-defined node plane along the diagonal. Subsequently increasing the frequency switched the nodal plane to a negative slope profile along the diagonal. At higher frequencies (e.g. 3.61 MHz) the nodal region was completely polarized in the xy plane.

B. Pressure Field in Microchannel using a Pyrex Reflector

In the case of the Pyrex reflector (see Figure 6), the lack of a strong pressure node in the range of 3 to 4 MHz indicated poorer acoustic confinement. Along the z-axis, the pressure nodes were spread across several frequencies, indicating a stronger dependence on frequency. Although a high degree of acoustic focusing may be achieved in one direction, the lateral direction may not be well confined, which was more pronounced for the Pyrex reflector. Here the acoustic pressure nodes were not as well-defined and even more dependent on

Figure 4. The composite piezoelectric structure (not to scale). The microchannel cross-section was 214 x 214 μm depicted in grey.
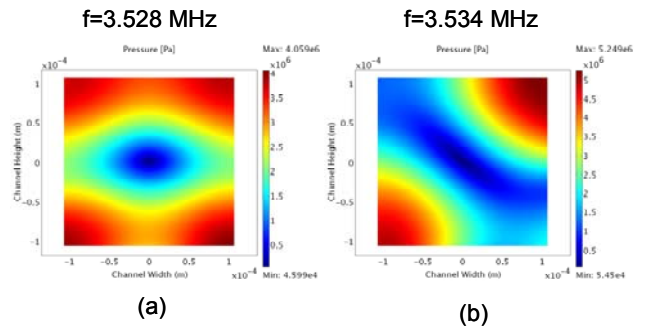

(a)　　　　　　(b)

Figure 5. Acoustic pressure field in the microchannel for the perfect reflector ($\partial p / \partial n = 0$) case. The channel height is oriented along the z-axis and channel width along the x-axis, where the y-axis is into the plane.

frequency since small changes (e.g. ±1 kHz) eliminated the nodes altogether. Above 3.55 MHz, multiple nodes were observed in the microchannel.
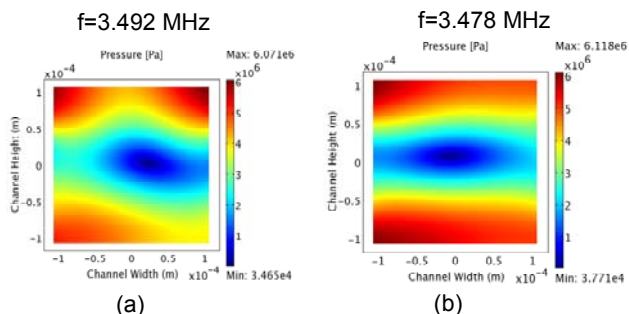

Figure 6. Acoustic pressure field in the microchannel for the Pyrex reflector case.

V. COEFFICIENT OF VARIANCE MEASUREMENTS

A. Drive Amplitude

As mentioned earlier, CV measurements were also made with a custom built confocal microscope. With these measurements, histograms (not shown) were created to understand the particle spread versus various metrics. The first metric assessed was the voltage used to drive the piezo transducer (Figure 7a). At lower drive voltages, a significant spread in the position of the particles was observed. And at higher drive voltages, there were significant deleterious
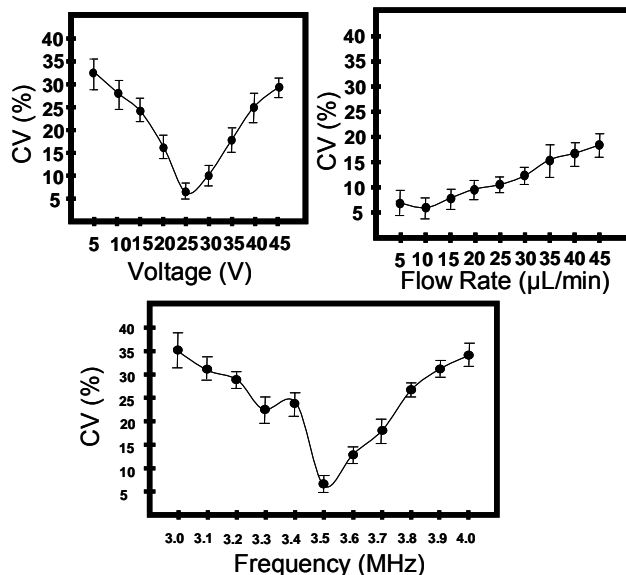

Figure 7. CV measurements versus transducer drive frequency, flow rates, and transducer drive frequency. The optimal operating point was 25Vpp drive signal, 10μl/min flow rate, and 3.48MHz drive signal. One variable was changed while the other two were kept at the optimal value. (a) CV measurements as a function of transducer drive voltage (b) CV measurements as a function of flow rates (c) CV measurements as a function of transducer drive frequency.

cavitation effects. For this device, the optimal drive voltage was $25V_{p-p}$.

B. Flow Rates

Flow cytometry histograms were also created to understand the particle spread versus flow rates (see Figure 7b). In these experiments, a broad range of acceptable flow rates seemed to suggest an upper bound but really no lower bound. The residence time within the channel was not an issue because the channels were very long-on the order of millimeters- and the entire channel resonates in these devices. At 500ul/min, the Reynolds number in the channel was around 40 and the flow started to shift to turbulent flow. However, the optimal flow rate was significantly less at10μl/min.

C. Drive Frequency

Finally, these measurements were made with regard to the transducer drive frequency (Figure 7c). In these devices, mainly the dimensions of the channels determine the frequency of operation. But due to variations in the fabrication processes, stray structural modes, and differences in transducer elements, there are shifts in the frequency of operation compared to what is expected from back of the envelope calculations. These devices were extremely sensitive to small frequency shifts, of 100kHz and below. The data suggest that the optimal operating frequency was around 3.48MHz.

VI. DISCUSSION

CV measurements from fluorescent emission intensities showed high spatial confinement of the particles. Cavitation was a significant problem at higher transducer drive amplitudes; fortunately, at frequencies of 1MHz and up, the threshold power required to generate a cavitation nucleus is fairly large. In addition, the device was not as sensitive to flow rates as it was to the other two metrics. Very low flow rates (<5μl/min) produced slightly higher CVs than the optimal operating point of 10μl/min. Finally, as the model and the experimental results suggest, the device is very sensitive to small shifts in frequency and, therefore, it is important to choose the frequency properly.

REFERENCES

[1] W. T. Coakley, J. J. Hawkes, M. A. Sobanski, C. M. Cousins, and J. Spengler, "Analytical scale ultrasonic standing wave manipulation of cells and microparticles," Ultrasonics, vol. 38, pp. 638-641, 2000.

[2] A. Haake and J. Dual, "Micro-manipulation of small particles by node position control of an ultrasonic standing wave," Ultrasonics, vol. 40, pp. 317-322, 2002.

[3] N.R. Harris, M. Hill, S. Beeby, Y. Shen, N.M. White, J.J. Hawkes and W.T. Coakley, "A silicon microfluidic ultrasonic separator," Sensors and Actuators B, vol. 95, pp.425-434, 2003.

[4] J.J. Hawkes and W.T. Coakley, "Force field particle filter combining ultrasound standing waves and laminar flow," Sensors and Actuators B, vol. 75, pp.213-222, 2001.

[5] A. Nilsson, F. Petersson, H. Jonsson, and T. Laurell, "Acoustic control of suspended particles in microfluidic chips," Lab on a Chip, vol. 4, pp.131-135,2004